



Enhancement of second-order optical nonlinearities and nanoscale periodic domain patterning in ferroelectric boron-substituted aluminum nitride thin films

ALBERT SUCEAVA,¹  JOHN HAYDEN,¹ KYLE P. KELLEY,² 
YIHUANG XIONG,¹ BENAZIR FAZLIOGLU-YALCIN,¹ ISMAILA DABO,¹
SUSAN TROLIER-MCKINSTRY,¹ JON-PAUL MARIA,¹ AND
VENKATRAMAN GOPALAN^{1,3,4,*} 

¹Department of Materials Science and Engineering and the Materials Research Institute, The Pennsylvania State University, University Park, PA 16802, USA

²Center for Nanophase Materials Sciences, Oak Ridge National Laboratory, Oak Ridge, TN 37831, USA

³Department of Physics, Pennsylvania State University, University Park, PA, 16802, USA

⁴Department of Engineering Science and Mechanics, Pennsylvania State University, University Park, PA, 16802, USA

*vxg8@psu.edu

Abstract: The discovery and development of CMOS-compatible, nonlinear optical materials is essential to produce integrated photonic devices with advanced functionalities. AlN is a strong candidate for on-chip device demonstration due to its intrinsic second-order optical nonlinearities, large bandgap, and well-established fabrication techniques. However, AlN is not easily phase matched for the largest coefficient d_{33} ; the coefficients that could potentially be dispersion phase-matched, d_{31} and d_{15} , have weak nonlinearities. This work investigates ferroelectric $\text{Al}_{1-x}\text{B}_x\text{N}$ ($x = 0$ to 0.11) for viability as a large bandgap nonlinear optical material with unique suitability towards ultraviolet light generation using second harmonic generation. The linear and nonlinear optical properties are characterized accounting for material anisotropy. With increasing B concentration, a large enhancement from near negligible values to $d_{31} = 0.9 \pm 0.1$ pm/V and $d_{15} = 1.2 \pm 0.1$ pm/V is observed. This compares favorably to other large bandgap materials like $\beta\text{-Ba}(\text{BO}_2)_2$, where the largest nonlinear coefficient is $d_{22} \sim 2.3$ pm/V at 800 nm. This is accompanied by a change in the bandgap from 6.1 eV to 5.8 eV as B substitution goes from 0 to 11%. A periodically poled, quasi-phase-matched ferroelectric domain pattern with 400 nm domain size and a wall roughness of <16 nm is demonstrated.

© 2023 Optica Publishing Group under the terms of the [Optica Open Access Publishing Agreement](#)

1. Introduction

Integrated photonics represents an area of growing technological significance with applications in telecommunications, metrology, biological imaging, and next-generation computing [1–12]. Replacement of traditional electronic processes with on-chip generation and manipulation of optical signals necessitates the discovery and maturation of CMOS-compatible optical materials. While major strides have been made in silicon (Si) based photonics, including demonstrations of optical phased arrays, ultrahigh-Q ring resonators, frequency combs, and hybrid integrated lasers, Si as a material platform is ultimately limited by its small bandgap and centrosymmetric structure resulting in negligible second-order optical nonlinearities [13–16]. Nonlinear optical (NLO) processes are essential for many complex operations in photonic devices, such as frequency conversion and generation through processes like sum and difference frequency generation and second harmonic generation (SHG) [17]. The linear electro-optic effect, or Pockels effect, is another significant nonlinear optical property used in electrically driven optical modulators

for long-distance optical communication and in quantum communication systems [18,19]. For nonlinear optical devices to function with high fidelity and efficiency, alternative material platforms must be considered with intrinsic properties favorable towards such ends.

Among thin film optical materials, aluminum nitride (AlN) occupies a major functional niche due to its large bandgap of 6.2 eV, appreciable second order nonlinearity ranging from 4-7 pm/V, and mature CMOS-compatible fabrication technology [20,21]. Consequently, sputtered AlN films have an established history in use for nonlinear photonic devices, with demonstrations including Kerr frequency combs, high Q factor microring resonators, electro-optic modulators, and integrated laser sources [22–26]. Despite these advantages, AlN still faces many limitations as an NLO material. Like other large bandgap NLO materials, the NLO properties of AlN are ultimately weak when compared to materials with bandgaps in the visible to infrared (IR) range, such as lithium niobate (LiNbO₃) which possesses a coefficient of $d_{33} = 25.2$ pm/V at a bandgap of 3.9 eV [27]. As a result, higher efficiency nonlinear optical materials with bandgaps suited for ultraviolet (UV) wavelengths are needed. Furthermore, AlN cannot be type I or type II intrinsically phase matched for UV light generation, a necessary condition for efficient generation in any frequency mixing process [28,29]. The absence of an intrinsic phase-matching condition has necessitated the use of waveguide dispersion engineering for efficient nonlinear processes [30–32]. This in turn, imposes additional design and manufacturing constraints and ultimately limits the application of AlN-based devices. Efforts to achieve quasi-phase matching by growing periodically poled AlN through control of surface termination has produced domain sizes as low as 600 nm [33]. However, the growth process results in the alternating domains having significantly different final heights and surface morphology, introducing sources of scattering loss and limiting waveguide performance [33,34]. More recently, it has been demonstrated that AlN thin films can indeed be switched as a ferroelectric under elevated temperatures, but optical devices based on this process have yet to be explored [35]. The development of aluminum scandium nitride (Al_{1-x}Sc_xN) as a ferroelectrically switchable derivative provided another viable way to pursue quasi-phase matching in AlN-based structures. Yoshioka et al. observed that Sc solid solution furthermore greatly enhances optical nonlinearities in AlN, albeit at the cost of a reduced optical bandgap, roughly a linear 15% decrease in the bandgap for every 10% Sc introduced [36,37]. In this work, the effect of boron (B) solid solution on the linear and nonlinear optical properties of ferroelectric Al_{1-x}B_xN is explored to develop a candidate material for nonlinear photonics in the UV range. In addition, switching of ferroelectric domains is demonstrated in order to achieve a periodically poled structure for quasi-phase matched generation of UV SHG using the largest SHG coefficient, d_{33} .

2. Fabrication

Al_{1-x}B_xN films with boron nitride (BN) concentrations ranging from 0 to 11% were grown by reactive magnetron sputtering in a custom multi-cathode vacuum chamber with a base pressure $< 3.0 \times 10^{-7}$ Torr at deposition temperatures. Prior to Al_{1-x}B_xN growth, 100 nm of tungsten (W) with exclusive 110 texture was deposited on *c*-axis Al₂O₃ substrates by direct current (DC) sputtering in argon (Ar) at 5.5 mTorr pressure, 400 °C substrate temperature, 4 cm target-to-substrate distance, and a target power density of 8 W/cm². After W deposition, the substrate temperature was reduced to 325 °C and allowed to stabilize for at least 30 minutes. Without breaking vacuum, Al_{1-x}B_xN films were deposited by simultaneous pulsed-DC sputtering and radio frequency (RF) sputtering from 2 in. diameter Al (99.9995%, Kurt J. Lesker) and BN (99.5%, Kurt J. Lesker) targets, respectively, at a distance of 10 cm from the substrate. A sputtering gas pressure of 2.0 mTorr was maintained while flowing 5 sccm Ar and 15 sccm N₂. The pulsed-DC parameters were held constant for all films at 250 W target power to the Al target, 100 kHz pulse frequency, and 1536 ns pulse length, while the BN target power was modulated from 0 to 112 W to control cation stoichiometry. Films were grown to a thickness of ~500 nm for

this study, with exact thicknesses for every sample determined using spectroscopic ellipsometry measurements described later in this work. As such, the bulk of the films can be considered fully relaxed. Knowledge of specific growth parameters needed to obtain a desired composition and thickness were developed from previous work on this material as reported in Hayden et al. [38]. Substitutional B concentrations reported in this study were measured using a Physical Electronics VersaProbe II x-ray photoelectron spectrometer (XPS) equipped with an Al K α source. To eliminate the effects of surface oxidation and adventitious carbon, measurements were performed after sputter cleaning the surface with a 3 keV Ar ion beam for 15 minutes. High resolution spectra of the B 1s and Al 2p orbitals were collected and integrated using Shirley backgrounds. Because of the low sensitivity of the B 1s peak, 5 scans were averaged to improve signal-to-noise. Integrated area ratios normalized with relative sensitivity factors from the CasaXPS software package were then used to calculate B concentration in the films, assuming a stoichiometric III:V ratio.

Phase purity and orientation preference of the sputtered films was verified by x-ray diffraction using copper (Cu) source radiation from a Malvern Panalytical Empyrean with the Bragg-Brentano HD incident optic and Pixel3D detector. The Al_{1-x}B_xN films used in this study have the wurtzite structure (Fig. 1(a)) and are fully *c*-axis oriented, as previously reported by Hayden et al. [38]. Figure 1(b) shows symmetric θ -2 θ scans of the Al_{1-x}B_xN (002), W (110), and Al₂O₃ (006) reflections for films with $x = 0.00, 0.02, 0.06, 0.11$. A shift of the Al_{1-x}B_xN (002) peak to higher 2 θ values with increasing B concentration indicates a reduction in the *c*-axis lattice parameter from B substitution in the lattice, while relatively constant peak intensities for the B-substituted films demonstrates a high degree of crystallinity even for the highest concentrations of B used in this study. Rocking curve full width half maximum values were less than 2° for all films synthesized. A more detailed discussion on structural parameters for films grown using this process, including exact lattice parameters and epitaxial registry, is reported in Hayden et al. [38].

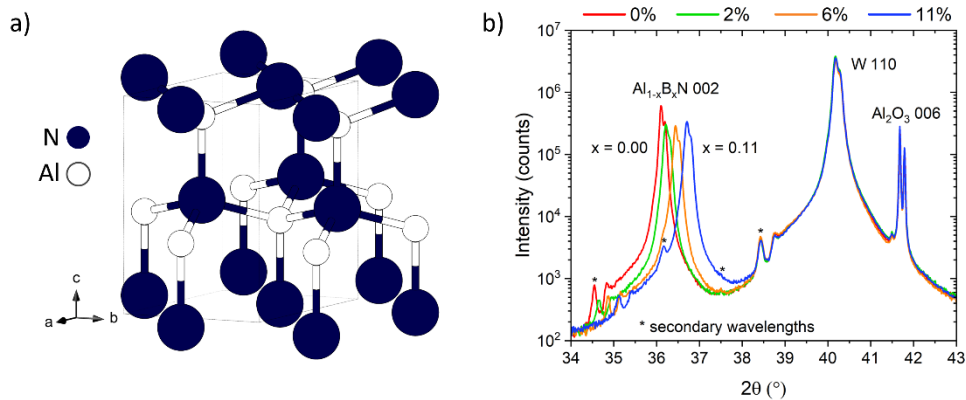


Fig. 1. a) Wurtzite structure of AlN. In Al_{1-x}B_xN, B substitutes Al on a cation site. b) XRD symmetric θ -2 θ scans of Al_{1-x}B_xN composition series used in this study.

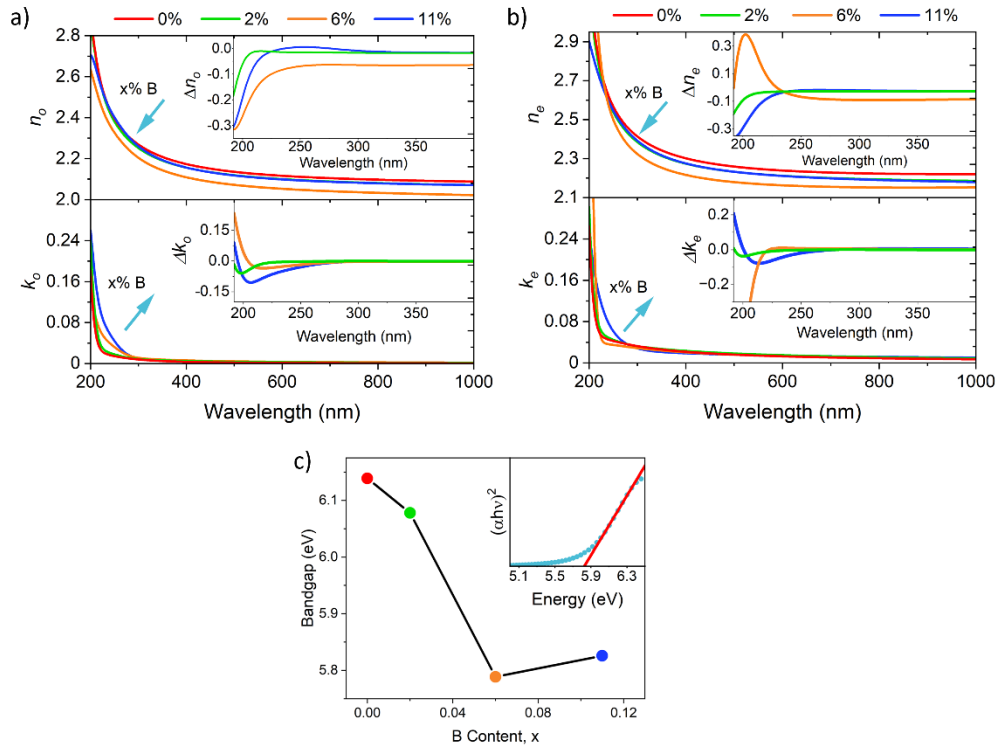


Fig. 2. Complex ordinary (a) and extraordinary (b) indices of refraction of $\text{Al}_{1-x}\text{B}_x\text{N}$ determined. (Inset) Difference between index values of AlN film and B-substituted $\text{Al}_{1-x}\text{B}_x\text{N}$, Δn_i and Δk_i . (c) Bandgap of $\text{Al}_{1-x}\text{B}_x\text{N}$ determined from Tauc analysis (inset) of extinction coefficients.

3. Results and discussion

3.1. Spectroscopic ellipsometry measurement and birefringent indices of refraction

The linear optical properties of $\text{Al}_{1-x}\text{B}_x\text{N}$ were characterized using a Woollam M2000 variable angle spectroscopic ellipsometer in conjunction with a Woollam M-2000XF-193 fixed angle ellipsometer. The variable angle ellipsometer provided a wavelength range of 246-1690 nm and measurements at 4 angles of incidence: 45° , 55° , 65° and 75° . Mueller matrix measurements at multiple angles of incidence allowed for a birefringent model to be constructed for the measured wavelengths. The wavelength range investigated by the fixed angle ellipsometer was 192-1000 nm and the measurements were performed at 65° incidence. This allowed the optical properties near the band edge of the material to be evaluated and the bandgap to be determined.

The dielectric function of the composition series was fit using a combination of Herzinger-Johs parameterized semiconductor oscillators (Psemi) and Gaussian oscillators with UV and IR poles included [39–41]. The Psemi oscillator functions allow for the imaginary part of the dielectric function to be fit using an oscillator profile constructed of 4 polynomial splines that remains Kramers-Kronig consistent. A detailed description of the fitting parameters and a table of fit parameters employed is included in the [Supplement 1](#) document. After initial construction of this model over the range of 246-1690 nm using multiple angles of incidence to capture material anisotropy, the fit was converged for the wavelength range of 192-1000 nm. Measurements were also performed on *c*-axis oriented Al_2O_3 and 100 nm W/ Al_2O_3 substrates. This allowed a model to be constructed sequentially for the entire film stack of each sample. Surface roughness values

collected from atomic force microscope (AFM) measurements were incorporated into the model as an additional surface Bruggeman effective medium approximation (EMA) layer composed of 50% void and 50% $\text{Al}_{1-x}\text{B}_x\text{N}$. The thickness of the EMA layer was directly taken as the RMS surface roughness values obtained from the AFM scans, with images presented in the Supplement 1 document Fig. S1. These surface roughness values are 2.5 nm, 3.9 nm, 7.9 nm, and 3.3 nm for the $x = 0.00, 0.02, 0.06,$ and 0.11 $\text{Al}_{1-x}\text{B}_x\text{N}$ films respectively.

Analysis of the extracted optical constants for the composition series reveal a simultaneous decrease in the ordinary and the extraordinary indices of refraction with increasing boron concentration, as shown in Fig. 2. Similarly, an increase in the extinction coefficient at a given wavelength can be seen with increasing boron concentration near the band edge, suggesting a reduction in bandgap. All the films are highly transparent from the band edge out to 1690 nm. Using the extinction coefficients obtained via ellipsometry, the absorption coefficients were obtained. A Tauc analysis, plotting $(\alpha h\nu)^2$ vs $h\nu$, was used to determine the direct allowed transitions present in $\text{Al}_{1-x}\text{B}_x\text{N}$ [42]. Tauc analysis confirmed a reduction in bandgap with B incorporation, resulting in a change from 6.1 eV to 5.8 eV at the highest B concentration measured, similar to initial specimens measured by Hayden et al. [38]. Individual Tauc plots for each $\text{Al}_{1-x}\text{B}_x\text{N}$ sample are provided in Supplemental Fig. S2.

3.2. Second harmonic generation from $\text{Al}_{1-x}\text{B}_x\text{N}$

The second order NLO susceptibility of $\text{Al}_{1-x}\text{B}_x\text{N}$ was studied via SHG polarimetry using a fundamental wavelength of 800 nm and the resulting second harmonic at 400 nm, as depicted in Fig. 3(a). The choice of wavelengths ensured minimal optical loss to absorption; thus, any SHG measured from the sample was non-resonant. The 800 nm light was generated by a Spectra-Physics Solstice Ace amplified Ti:Sapphire laser with a 1 kHz repetition rate and 100 fs pulse width. Light was focused onto the sample using a 10 cm focal length lens, producing a spot size 50 μm in diameter as determined by knife-edge measurements. The SHG process is described by the equation where $i, j,$ and k describe directions along the crystal physics axes. For wurtzite $\text{Al}_{1-x}\text{B}_x\text{N}$ with point group $6mm$, the Z_1 and Z_3 crystal physics axes are aligned with the [100] and [001] crystallographic directions respectively, with the Z_2 axis perpendicular to Z_1 and Z_3 such that they form a right-handed coordinate set. The polarization of the incident light is rotated using a half-wave plate such that the electric field vector is described as $E^\omega = (E^\omega \cos \theta \cos \varphi, E^\omega \sin \varphi, E^\omega \cos \theta \sin \varphi)$ in the crystal physics coordinate system, where θ is the angle of incidence and φ describes the rotation of the polarization with 0 lying along the Z_1 direction at normal incidence. SHG light was further separated into s and p-polarized components using an analyzer before the 800 nm fundamental was filtered out and the remaining signal detected using a photomultiplier tube. Detailed discussions and schematics of SHG polarimetry setups may be found in Ref. [43]. Measurements were performed in reflection geometry at incident angles of 45° and 60° so that all elements of the second harmonic tensor were obtained. For the point group $6mm$, the second harmonic tensor appears in Voigt notation as:

$$d_{ijk} = \begin{pmatrix} 0 & 0 & 0 & 0 & d_{15} & 0 \\ 0 & 0 & 0 & d_{15} & 0 & 0 \\ d_{31} & d_{31} & d_{33} & 0 & 0 & 0 \end{pmatrix}$$

resulting in 3 independent elements.

Numerical equations for the generated second harmonic intensity, accounting for wave propagation at interfaces and multireflection phenomena, were generated using the #SHAARP open-source package to model the second harmonic response of anisotropic materials. The model was modified to account for multilayer reflections of both the fundamental and SHG waves [44]. The SHG coefficients d_{31} and d_{15} were assumed to be independent, as the presence of

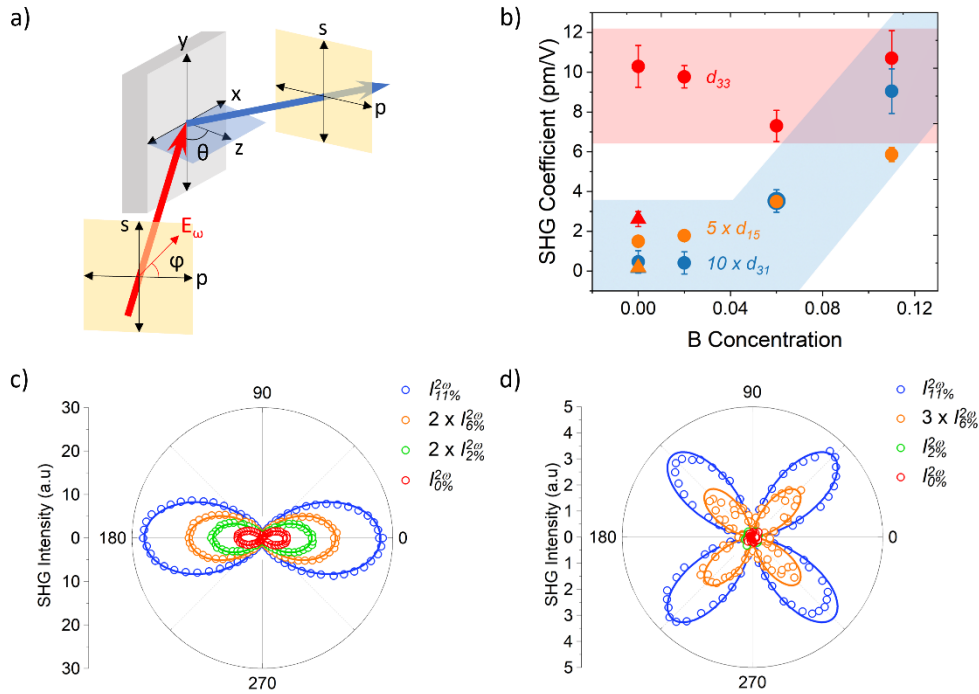


Fig. 3. (a) Schematic of SHG polarimetry experimental geometry. (b) Extracted SHG coefficients from $\text{Al}_{1-x}\text{B}_x\text{N}$ (circles) and an AlN single crystal (triangle). Polar plots of p-polarized (c) and s-polarized SHG (d) from $\text{Al}_{1-x}\text{B}_x\text{N}$, with experimental data shown as open circles and fitting curves overlaid. Some intensities have been scaled to improve visibility, but relative ordering remains consistent.

noticeable dispersion at the wavelengths of measurement prohibit the assumption of Kleinman symmetry [17]. Complex indices of refraction required to generate the fitting equations were taken from the material dispersion curves obtained using spectroscopic ellipsometry. Due to rigorous handling of multireflection effects and the general cubic dependence of the second order nonlinear susceptibility on the linear susceptibility, inaccuracy in the indices of refraction used represent the largest possible source of error in this analysis [17]. However, the accuracy of the spectroscopic ellipsometry measurements performed is to ± 0.001 , and thus error in this regard is expected to be minimal. The resulting output of the #SHAARP package is a set of numerically solved equations describing generated second harmonic light at a chosen incident angle, with only d_{31} , d_{33} , d_{15} , and the polarization angle, ϕ , as unknowns. The full form fitting equations generated are provided in the Supplemental Table 2 along with a detailed discussion of the fitting process. A generic scaling factor was assigned to each fitting equation to encapsulate the incident power and geometric considerations like the focusing condition during the experiment. To calibrate this scaling factor, a reference X-cut LiNbO_3 single crystal was measured under identical experimental conditions. The LiNbO_3 calibration sample was obtained from MTI Corporation; its SHG coefficients were provided by the manufacturer. SHG coefficients were extracted from simultaneous fits of s and p-polarized polarimetry data at all angles of incidence measured to yield the results in Fig. 3(b). Representative polarimetry plots taken at 60° incidence are displayed in Fig. 3(c-d), demonstrating an overall increase in raw SHG signal from films with increasing B concentration. Measured coefficients from the pure AlN film were $d_{33} = 10.3 \pm 1.1$ pm/V, $d_{31} = 0.05 \pm 0.05$ pm/V, and $d_{15} = 0.3 \pm 0.06$ pm/V. Such values are consistent with other reported SHG coefficients in sputtered AlN films, with values ranging from $d_{33} = 4$ pm/V to $d_{33} = 11 \pm 1$

pm/V, and $d_{31} = 0.04$ pm/V to $d_{31} = 0.28$ pm/V [45–48]. In addition, a sample of single crystal AlN was measured and analyzed using the same theoretical framework. The AlN single crystal measured was a bulk substrate obtained from Crystal IS, a commercial supplier of AlN-based optoelectronics. Extracted SHG coefficients of the AlN single crystal were $d_{33} = 2.6 \pm 0.4$ pm/V, $d_{31} = 0.01 \pm 0.02$ pm/V, and $d_{15} = 0.04 \pm 0.02$ pm/V, in comparison to values of $d_{33} = 4.3 \pm 0.3$ pm/V and $d_{31} = 0.1$ pm/V reported in literature [45]. One possible reason for the discrepancy in measured SHG values could be the quality of the crystal; the crystal we measured may have more defects, as suggested by a much larger absorption coefficient at the wavelength of measurement than the AlN single crystal measured and reported on in previous literature. The suspected higher concentrations of defects present may be supported by observation of the sample under an optical microscope, where bright, light-scattering spots can be seen at a high density throughout the bulk of the sample as shown in supplemental Fig. S3.

Much of the enhancement of the total SHG generated in the $\text{Al}_{1-x}\text{B}_x\text{N}$ films can be attributed to increases in d_{31} and d_{15} , while d_{33} remained relatively unchanged with B solid solution; any variation is attributed to variations in the film synthesis. This is most prominently displayed in the *s*-polarized polar plots, where the intensity is solely proportional to $d_{15} \cos \varphi \sin \varphi$. It can be seen that with B substitution, d_{15} changes from an indeterminably low value in pure AlN to $d_{15} = 1.2 \pm 0.07$ pm/V in $\text{Al}_{0.89}\text{B}_{0.11}\text{N}$ at 800 nm. For comparison, this is on the same order as the effective SHG coefficient in phase-matched $\beta\text{-Ba}(\text{BO}_2)_2$ for 800 nm generation: $d_{\text{eff}} \sim 2.1$ pm/V [49]. Enhancement of d_{31} suggests the emergence of a nonlinear polarization component along the Z_3 direction in response to electric fields in the Z_1 direction; enhancement in the d_{15} suggests an emergence of a nonlinear polarization component in the Z_1 direction in response to simultaneous fields in the Z_1 and Z_3 directions. To investigate the mechanism behind this observed enhancement of the coupling between the Z_1 and Z_3 directions, first-principles calculations were employed to generate models representing energy minimized structures at varying B concentrations.

The first-principles calculations were performed using the Vienna ab initio simulation package (VASP) with the projector augmented wave (PAW) method [50,51]. The structure optimization is carried out using the generalized gradient approximation (GGA) with the Perdew-Burke-Ernzerhof (PBE) functional [52]. The energy cutoff is set to 520 eV, and the Brillouin zone is sampled by a Γ -centered Monkhorst-Pack grid of $2 \times 2 \times 2$. The atomic positions and the lattice vectors are fully optimized until the forces on the ions are smaller than 0.01 eV/Å. The van der Waals interactions are also incorporated using the DFT-D3 method, which has been shown to correctly predict hexagonal BN as the most stable phase, as reported previously [38,53]. The ground-state energy is obtained by solving the Kohn-Sham (KS) equations self-consistently. Each equation describes the single-particle wave functions:

$$\left[-\frac{1}{2} \nabla_i^2 + V_{\text{ext}}(\mathbf{r}) + V_{\text{H}}(\mathbf{r}) + V_{\text{xc}}(\mathbf{r}) \right] \psi_i(\mathbf{r}) = \varepsilon_i \psi_i(\mathbf{r})$$

On the left-hand side of the KS equation, each term stands for kinetic energy, the KS potential that includes the potential terms of external potential $V_{\text{ext}}(\mathbf{r})$, Hartree $V_{\text{H}}(\mathbf{r})$, and the exchange-correlation $V_{\text{xc}}(\mathbf{r})$. To simulate the various B compositions, a 72-atom AlN wurtzite supercell was used and then B was incorporated on the Al sites with an incremental percentage of 11%. The distributions of the B atoms were created by the special quasirandom structure (SQS) method that is implemented in the Alloy Theoretical Automated Toolkit (ATAT) package [54]. SQS cells are constructed to best approximate the random alloys using a finite-size supercell. The SQS construction follows the work of Van de Walle [53] to minimize the objective function Q :

$$Q = -\omega L + \sum_{\alpha} \left| \Gamma_{\alpha} - \Gamma_{\alpha}^{\text{target}} \right|,$$

where ω -weighted L stands for the largest length for all clusters such that $\Gamma_\alpha - \Gamma_\alpha^{\text{target}} = 0$. Γ_α and $\Gamma_\alpha^{\text{target}}$ are the components of the cluster vector and the target values, respectively. The summation covers the entire sets of cluster α .

The presence of B in the AlN wurtzite structure is observed to facilitate local distortion of the AlN₄ tetrahedra, as depicted in Fig. 4(a). Specifically, B atoms displace within the a - b crystallographic plane, such that the vertical B-N bonds along the c -axis in an ideal wurtzite structure are deflected away from the c -axis. When multiple B-centered tetrahedra are located adjacent to each other, this deflection of the bond away from the c -axis can be as high as 13-19°, as was observed in the 22%, 33%, and 44% B structures. In such extreme cases, the deflection of the B atom primarily serves to drive the coordination environment away from a tetrahedral geometry and towards a trigonal planar geometry reminiscent of a hexagonal BN structure. The accumulated effect of such local distortions in the wurtzite structure is an increased projection of the bond moments along the Z₁ and Z₂ directions and a reduction in the projections along the Z₃ direction within the simulated supercell.

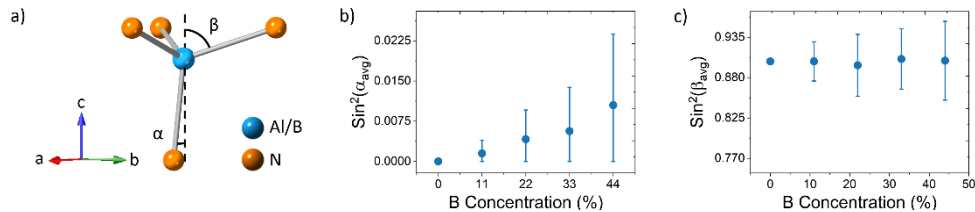


Fig. 4. (a) Schematic of distorted nitrogen tetrahedra observed in DFT-modeled structures. The angles of interest, α and β , are defined as the angle between an ideally c -axis oriented bond or a basal plane bond respectively, and the c -axis. (b) $\text{Sin}^2(\alpha)$ and (c) $\text{Sin}^2(\beta)$ of the average of the respective angle observed across all simulated tetrahedra, as a function of B inclusion. Error bars were drawn from the standard deviation in observed distorted angles.

The bond-charge model predicts the nonlinear susceptibility of a compound; this model has been successfully applied to many materials, including III-V compounds such as GaAs, GaP, and InSb [55]. In the model, the nonlinear susceptibility of a material can be derived from the nonlinear susceptibilities of its individual constituent bonds. The susceptibilities are then summed along a certain direction after multiplication with the appropriate direction cosines to obtain direction-dependent susceptibilities and individual SHG tensor elements. In the heavily substituted Al_{1-x}B_xN structures that were examined, a similar reasoning can be applied to understand that as bonds deflect away from purely c -oriented to having projections along both the a and c directions, nonlinear susceptibilities coupling the Z₁ and Z₃ directions, such as d_{31} and d_{15} will be increased. On the other hand, coefficients that relate solely to fields and induced polarizations along the Z₃ direction, namely d_{33} , may slightly decrease. From the examined bond angles in the simulated structures, it can be observed that there is a consistent canting of c -axis oriented bonds as B substitution increases, as shown in Fig. 4(b). The extent of such distortions is observed to increase nonlinearly in the simulated structures. That is, as more B is added to the AlN wurtzite structure, the magnitude of the local distortions increases nonlinearly in a similar fashion to how d_{31} and d_{15} are enhanced. Meanwhile, for bonds with nitrogen that comprise the basal planes of the wurtzite structure, no clear trend suggesting either a flattening or sharpening of the tetrahedra base emerges, as in Fig. 4(c). From this, it is qualitatively concluded that the local distortions in the direction of ideally c -axis oriented bonds are likely the primary contributor to the enhancement of nonlinear optical coefficients coupling fields and polarizations in the Z₁ and Z₃ directions, namely d_{31} and d_{15} .

3.3. Poling $Al_{1-x}B_xN$ for quasi-phase-matching

To demonstrate the potential for $Al_{1-x}B_xN$ in applications involving nonlinear generation of UV light, phase-matching viability was investigated. Due to intrinsic material dispersion, there generally exists a mismatch in the wavevectors for the fundamental pump light and generated second harmonic. Therefore, the co-propagating beams will eventually become out of phase and destructively interfere, limiting the total second harmonic power that can be generated, as depicted in Fig. 5(a) [17]. In strongly birefringent materials, type I phase matching occurs when $n_e^\omega = n_o^{2\omega}$, where n_o is the ordinary index of refraction and n_e the extraordinary index. In positive uniaxial materials, type II phase matching occurs when $[n_e^\omega + n_o^\omega]/2 = n_o^{2\omega}$ [28]. When met, these conditions eliminate the wavevector mismatch and potential for destructive interference between the fundamental and second harmonic wave, resulting in a quadratic increase in generated second harmonic power along the length of propagation. For the $Al_{1-x}B_xN$, series studied, no composition can be intrinsically phase-matched for a fundamental wavelength longer than 450 nm. However, the introduction of ferroelectric switchability allows for quasi-phase-matched structures, where domains are inverted every coherence length, defined as $\pi/\Delta k$, where Δk is the wavevector mismatch. Higher order quasi-phase-matching can occur when domains are inverted at higher multiples of the coherence length, still enabling efficient harmonic generation when domain size is a constraint. The exact domain periodicity required for quasi-phase-matching can be calculated from the condition $n^{2\omega} - n^\omega = N \frac{\lambda}{2\Lambda}$, where N is the order of the phase-matching scheme, λ the fundamental wavelength, and Λ the periodicity of the structure. This is shown in Fig. 5(b). The consequence of switching a ferroelectric domain is a physical reorientation of the structure such that the polar axis is mirrored across a plane normal to the switching direction. In the wurtzite $Al_{1-x}B_xN$ structure, this manifests as the N tetrahedra flipping orientation as an Al ion is pushed through the N basal plane [56]. The resulting transformation is that of the crystal physics Z_3 axis to $-Z_3$ such that the sign of the amplitude of the fundamental beam is switched with respect to the crystal physics coordinate system of the material. If performed at the appropriate interval, a full change in the phase of the generated second harmonic by π can be achieved to ensure that SHG is continually generated constructively [29].

To produce a quasi-phase-matched structure in $Al_{1-x}B_xN$, a piezoresponse force microscopy (PFM) tip was used to apply a voltage through a 20 nm thick film and manually pole domains into a desired structure. Here, a ± 15 V bias to the PFM tip was applied while grounding the W bottom electrode, with polarity of the bias dependent on the desired polarity of the region. Figure 5(c) shows the resulting band-excitation PFM amplitude (left panel) and phase (right panel) where clear c -axis oriented domains with alternating polarity and lengths of 400 nm can be observed. The domain wall RMS roughness is sub-pixel, where every pixel resolved is 15.6 nm, suggesting a domain wall roughness below this limit. All piezoresponse force microscopy measurements were captured using Budget Sensor Multi75E-G Cr/Pt coated AFM probes (~ 3 N/m). Band excitation was achieved by coupling the AFMs with an arbitrary wave generator and data acquisition electronics based on a National Instruments fast DAQ card. Custom software was used to generate the probing signal and store local BE and hysteresis loops. All band excitation PFM measurements were collected using frequencies ranging from 300-400 kHz at $2V_{AC}$, with subsequent simple harmonic oscillator fits applied to the collected spectra to extract amplitude and phase at the resonance frequency. All band excitation measurements were acquired using a Bruker Dimension Icon fitted inside a MBRAUN MB200B series glovebox (Ar filled, < 0.1 ppm O_2 , < 0.1 ppm H_2O). Post poling images were acquired directly after DC writing with a PFM tip bias of ± 15 V.

The periodicity was chosen to nearly match the condition for first order quasi-phase-matching when using a 450 nm fundamental for generation of 225 nm UV light in $Al_{0.89}B_{0.11}N$. Robust polarization reversal can be observed, demonstrating strong viability for ferroelectric domain engineering in $Al_{1-x}B_xN$ -based photonic devices. The metallic W layer beneath the poled

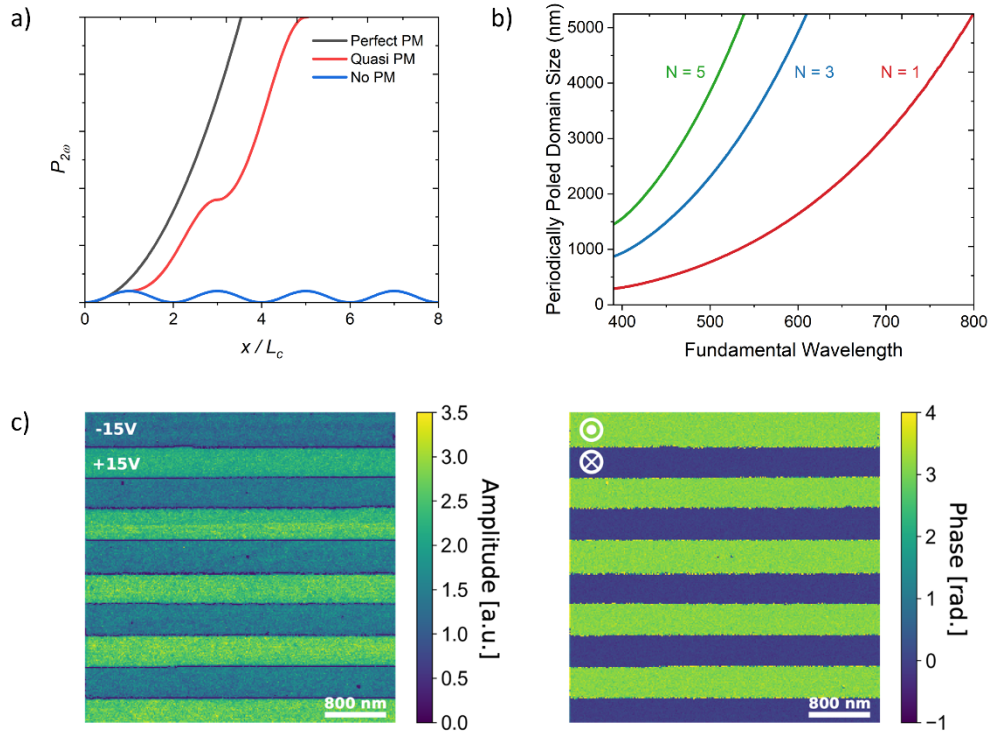


Fig. 5. (a) Schematic of second harmonic power generated as a function of propagation distance in a material with perfect, quasi, and no phase matching. (b) Periodically poled domain size required for N^{th} order quasi phase matching in $\text{Al}_{0.89}\text{B}_{0.11}\text{N}$. (c) Band-excitation PFM amplitude (left panel) and phase (right panel) showing periodically poled domains patterned via ± 15 V DC bias applied to the PFM tip. Domains are 400 nm in width.

film prevented the coupling of light and direct measurement of efficiently generated SHG and propagation losses. Poling thicker films and transferring poled films onto alternative substrates will promote efficient UV light generation from a smooth, AlN-based waveguide. While the film chosen for this demonstration was only 20 nm, the coercive field of $\text{Al}_{0.89}\text{B}_{0.11}\text{N}$ is roughly 5.5 MV/cm, and thus domain reversal in a 500 nm thick film would require 275 V which is certainly feasible using traditional electrode masks [38].

4. Conclusions

The dependence of the linear and nonlinear optical properties of $\text{Al}_{1-x}\text{B}_x\text{N}$ on B concentration was systematically investigated. The effect of B inclusion on the ordinary and extraordinary refractive indices of $\text{Al}_{1-x}\text{B}_x\text{N}$ is weak. However, a decrease in ordinary and extraordinary indices of refraction, along with a reduction of the bandgap is observed. Second harmonic generation from the material was observed to increase monotonically with B concentration, primarily due to an enhancement of the d_{31} and d_{15} SHG coefficients. The largest SHG coefficient, d_{33} , remained relatively unchanged with B doping. To demonstrate the feasibility of exploiting the ferroelectric behavior of $\text{Al}_{1-x}\text{B}_x\text{N}$ towards quasi-phase-matched generation of UV light, a periodically poled structure was written using a PFM tip with domain sizes down to 400 nm and very straight domain walls with wall roughness of < 16 nm. This pattern could quasi-phase match fundamental light of 450 nm into UV light of 225 nm. The patterned structure displayed

well-defined domain boundaries between oppositely poled *c*-axis oriented domains, indicating potential for waveguides based on quasi-phase-matching the largest SHG coefficient, d_{33} .

Funding. U.S. Department of Energy (DE-SC0020145, DE-SC0021118).

Acknowledgments. The growth, optical characterization, and first principles modeling of this material is based upon work supported by the center for 3D Ferroelectric Microelectronics (3DFeM), an Energy Frontier Research Center funded by the U.S. Department of Energy, Office of Science, Office of Basic Energy Sciences Energy Frontier Research Centers program under Award Number DE-SC0021118. The piezoresponse force microscopy research was performed at Oak Ridge National Laboratory's Center for Nanophase Materials Sciences (CNMS), a U.S. Department of Energy, Office of Science User Facility. B.F.-Y. acknowledges the US Department of Energy, Office of Science, Basic Energy Sciences, under Award Number DE-SC0020145 as part of the Computational Materials Sciences Program. We would like to acknowledge Rui Zu for providing his personal #SHAARP code for analysis of the optical second harmonic generation data collected for this work, as well as for multiple discussions regarding modelling and interpretation of said results. J-P.M. and V.G. acknowledge valuable discussions with Joseph Mantese from Raytheon.

Disclosures. All authors declare no conflict of interest.

Data availability. Data underlying the results presented in this paper are not publicly available at this time but may be obtained from the authors upon reasonable request.

Supplemental document. See [Supplement 1](#) for supporting content.

References

1. Y. Qi and Y. Li, "Integrated lithium niobate photonics," *Nanophotonics* **9**(6), 1287–1320 (2020).
2. Z. Sun, Y. Li, B. Bai, Z. Zhu, and H. Sun, "Silicon nitride-based Kerr frequency combs and applications in metrology," *Adv. Photonics* **4**(06), 064001 (2022).
3. P. Wang and B. L. Miller, "Waveguide-enhanced raman spectroscopy (WERS): an emerging chip-based tool for chemical and biological sensing," *Sensors* **22**(23), 9058 (2022).
4. E. Polino, M. Valeri, N. Spagnolo, and F. Sciarrino, "Photonic quantum metrology," *AVS Quantum Science* **2**(2), 024703 (2020).
5. N. L. Kazanskiy, S. N. Khonina, and M. A. Butt, "Advancement in silicon integrated photonics technologies for sensing applications in near-infrared and mid-infrared region: a review," *Photonics* **9**(5), 331 (2022).
6. V. M. N. Passaro, C. de Tullio, B. Troia, M. la Notte, G. Giannoccaro, and F. de Leonardis, "Recent advances in integrated photonic sensors," *Sensors* **12**(11), 15558–15598 (2012).
7. F. Kish, V. Lal, and P. Evans, *et al.*, "System-on-Chip Photonic Integrated Circuits," *IEEE J. Select. Topics Quantum Electron.* **24**(1), 6100120 (2018).
8. B. J. Shastri, A. N. Tait, T. Ferreira de Lima, W. H. P. Pernice, H. Bhaskaran, C. D. Wright, and P. R. Prucnal, "Photonics for artificial intelligence and neuromorphic computing," *Nat. Photonics* **15**(2), 102–114 (2021).
9. J. Wang, F. Sciarrino, A. Laing, and M. G. Thompson, "Integrated photonic quantum technologies," *Nat. Photonics* **14**(5), 273–284 (2020).
10. Y. Shen, N. C. Harris, S. Skirlo, M. Prabhu, T. Baehr-Jones, M. Hochberg, X. Sun, S. Zhao, H. Larochelle, D. Englund, and M. Soljacic, "Deep learning with coherent nanophotonic circuits," *Nat. Photonics* **11**(7), 441–446 (2017).
11. A. W. Elshaari, W. Pernice, K. Srinivasan, O. Benson, and V. Zwiller, "Hybrid integrated quantum photonic circuits," *Nat. Photonics* **14**(5), 285–298 (2020).
12. T. L. Koch and U. Koren, "Semiconductor Photonic Integrated Circuits," *IEEE* **27**, 641 (1991).
13. A. L. Gaeta, M. Lipson, and T. J. Kippenberg, "Photonic-chip-based frequency combs," *Nat. Photonics* **13**(3), 158–169 (2019).
14. W. Bogaerts, P. de Heyn, T. van Vaerenbergh, K. de Vos, S. Kumar Selvaraja, T. Claes, P. Dumon, P. Bienstman, D. van Thourhout, and R. Baets, "Silicon microring resonators," *Laser Photonics Rev.* **6**(1), 47–73 (2012).
15. S. Li, D. Zhang, J. Zhao, Q. Yang, X. Xiao, S. Hu, L. Wang, M. Li, X. Tang, Y. Qiu, M. Luo, and S. Yu, "Silicon micro-ring tunable laser for coherent optical communication," *Opt. Express* **24**(6), 6341 (2016).
16. J. Sun, E. Timurdogan, A. Yaacobi, E. S. Hosseini, and M. R. Watts, "Large-scale nanophotonic phased array," *Nature* **493**(7431), 195–199 (2013).
17. Robert W. Boyd, *Nonlinear Optics* (Elsevier, 2003).
18. N. J. Lambert, A. Rueda, F. Sedlmeir, and H. G. L. Schwefel, "Coherent Conversion Between Microwave and Optical Photons—An Overview of Physical Implementations," *Adv. Quantum Technol.* **3**(1), 1900077 (2020).
19. A. Yariv and P. Yeh, *Optical Waves in Crystals: Propagation and Control of Laser Radiation* (Wiley, 2002).
20. X. Liu, A. W. Bruch, and H. X. Tang, "AlN nonlinear optics and integrated photonics," in *Semiconductors and Semimetals* (Academic Press Inc., 2021), 107, pp. 223–281.
21. N. Li, C. P. Ho, S. Zhu, Y. H. Fu, Y. Zhu, and L. Y. T. Lee, "Aluminium nitride integrated photonics: A review," *Nanophotonics* **10**(9), 2347–2387 (2021).
22. H. Jung and H. X. Tang, "Aluminum nitride as nonlinear optical material for on-chip frequency comb generation and frequency conversion," *Nanophotonics* **5**(2), 263–271 (2016).

23. X. Liu, C. Sun, B. Xiong, L. Wang, J. Wang, Y. Han, Z. Hao, H. Li, Y. Luo, J. Yan, T. Wei, Y. Zhang, and J. Wang, "Integrated High-Q Crystalline AlN Microresonators for Broadband Kerr and Raman Frequency Combs," *ACS Photonics* **5**(5), 1943–1950 (2018).
24. C. Xiong, W. H. P. Pernice, and H. X. Tang, "Low-loss, silicon integrated, aluminum nitride photonic circuits and their use for electro-optic signal processing," *Nano Lett.* **12**(7), 3562–3568 (2012).
25. X. Liu, C. Sun, B. Xiong, L. Wang, J. Wang, Y. Han, Z. Hao, H. Li, Y. Luo, J. Yan, T. Wei, Y. Zhang, and J. Wang, "Integrated continuous-wave aluminum nitride Raman laser," *Optica* **4**(8), 893 (2017).
26. T. J. Lu, B. Lienhard, K. Y. Jeong, H. Moon, A. Iranmanesh, G. Grosso, and D. Englund, "Bright High-Purity Quantum Emitters in Aluminum Nitride Integrated Photonics," *ACS Photonics* **7**(10), 2650–2657 (2020).
27. David N. Nikogosyan, *Nonlinear Optical Crystals: A Complete Survey* (Springer-Verlag, 2005).
28. W. Zhang, H. Yu, H. Wu, and P. S. Halasyamani, "Phase-Matching in Nonlinear Optical Compounds: A Materials Perspective," *Chem. Mater.* **29**(7), 2655–2668 (2017).
29. M. Houe and P. D. Townsend, *An Introduction to Methods of Periodic Poling for Second-Harmonic Generation* (IOP, 1995), 28.
30. D. N. Hahn, G. T. Kiehne, J. B. Ketterson, G. K. L. Wong, P. Kung, A. Saxler, and M. Razeghi, "Phase-matched optical second-harmonic generation in GaN and AlN slab waveguides," *J. Appl. Phys.* **85**(5), 2497–2501 (1999).
31. W. H. P. Pernice, C. Xiong, C. Schuck, and H. X. Tang, "Second harmonic generation in phase matched aluminum nitride waveguides and micro-ring resonators," *Appl. Phys. Lett.* **100**(22), 223501 (2012).
32. T. Troha, M. Rigler, D. Alden, I. Bryan, W. Guo, R. Kirste, S. Mita, M. D. Gerhold, R. Collazo, Z. Sitar, and M. Zgonik, "UV second harmonic generation in AlN waveguides with modal phase matching," *Opt. Mater. Express* **6**(6), 2014–2023 (2016).
33. D. Alden, W. Guo, R. Kirste, F. Kaess, I. Bryan, T. Troha, A. Bagal, P. Reddy, L. H. Hernandez-Balderrama, A. Franke, S. Mita, C.-H. Chang, A. Hoffmann, M. Zgonik, R. Collazo, and Z. Sitar, "Fabrication and structural properties of AlN submicron periodic lateral polar structures and waveguides for UV-C applications," *Appl. Phys. Lett.* **108**(26), 261106 (2016).
34. D. Alden, T. Troha, R. Kirste, S. Mita, Q. Guo, A. Hoffmann, M. Zgonik, R. Collazo, and Z. Sitar, "Quasi-phase-matched second harmonic generation of UV light using AlN waveguides," *Appl. Phys. Lett.* **114**(10), 103504 (2019).
35. W. Zhu, J. Hayden, F. He, J. I. Yang, P. Tipsawat, M. D. Hossain, J. P. Maria, and S. Trolier-McKinstry, "Strongly temperature dependent ferroelectric switching in AlN, Al_{1-x}Sc_xN, and Al_{1-x}B_xN thin films," *Appl. Phys. Lett.* **119**(6), 062901 (2021).
36. V. Yoshioka, J. Lu, Z. Tang, J. Jin, R. H. Olsson, and B. Zhen, "Strongly enhanced second-order optical nonlinearity in CMOS-compatible Al_{1-x}Sc_xN thin films," *APL Mater.* **9**(10), 101104 (2021).
37. R. Deng, S. R. Evans, and D. Gall, "Bandgap in Al_{1-x}Sc_xN," *Appl. Phys. Lett.* **102**(11), 112103 (2013).
38. J. Hayden, M. D. Hossain, Y. Xiong, K. Ferri, W. Zhu, M. V. Imperatore, N. Giebink, S. Trolier-McKinstry, I. Dabo, and J. P. Maria, "Ferroelectricity in boron-substituted aluminum nitride thin films," *Phys. Rev. Mater.* **5**(4), 044412 (2021).
39. C. M. Herzinger and B. D. Johs, Dielectric Function Parametric Model, and Method of Use, US Patent US5796983A (1998).
40. C. M. Herzinger, B. Johs, W. A. McGahan, J. A. Woollam, and W. Paulson, "Ellipsometric determination of optical constants for silicon and thermally grown silicon dioxide via a multi-sample, multi-wavelength, multi-angle investigation," *J. Appl. Phys. (Melville, NY, U. S.)* **83**(6), 3323–3336 (1998).
41. J. M. Khoshman, J. N. Hilfiker, N. Tabet, and M. E. Kordesch, "Multiple oscillator models for the optical constants of polycrystalline zinc oxide thin films over a wide wavelength range," *Appl. Surf. Sci.* **307**, 558–565 (2014).
42. J. Li, K. B. Nam, M. L. Nakarmi, J. Y. Lin, H. X. Jiang, P. Carrier, and S. H. Wei, "Band structure and fundamental optical transitions in wurtzite AlN," *Appl. Phys. Lett.* **83**(25), 5163–5165 (2003).
43. S. A. Denev, T. T. A. Lummen, E. Barnes, A. Kumar, and V. Gopalan, "Probing ferroelectrics using optical second harmonic generation," *J. Am. Ceram. Soc.* **94**(9), 2699–2727 (2011).
44. R. Zu, B. Wang, J. He, J. J. Wang, L. Weber, L. Q. Chen, and V. Gopalan, "Analytical and numerical modeling of optical second harmonic generation in anisotropic crystals using #SHAARP package," *npj Comput. Mater.* **8**(1), 246 (2022).
45. A. Majkić, A. Franke, R. Kirste, R. Schlessler, R. Collazo, Z. Sitar, and M. Zgonik, "Optical nonlinear and electro-optical coefficients in bulk aluminium nitride single crystals," *Phys. Status Solidi B* **254**(9), 1700077 (2017).
46. Y. Fujii, S. Yoshida, S. Misawa, S. Maekawa, and T. Sakudo, "Nonlinear optical susceptibilities of AlN film," *Appl. Phys. Lett.* **31**(12), 815–816 (1977).
47. G. T. Kiehne, G. K. L. Wong, and J. B. Ketterson, "Optical second-harmonic generation in sputter-deposited AlN films," *J. Appl. Phys. (Melville, NY, U. S.)* **84**(11), 5922–5927 (1998).
48. M. C. Larciprete, A. Bosco, A. Belardini, R. Li Voti, G. Leahu, C. Sibilìa, E. Fazio, R. Ostuni, M. Bertolotti, A. Passaseo, B. Poñ, and Z. del Prete, "Blue second harmonic generation from aluminum nitride films deposited onto silicon by sputtering technique," *J. Appl. Phys. (Melville, NY, U. S.)* **100**(2), 023507 (2006).
49. D. N. Nikogosyan, *Nonlinear Optical Crystals: A Complete Survey* (Springer-Verlag, 2005).
50. G. Kresse and J. Furthmüller, "Efficiency of ab-initio total energy calculations for metals and semiconductors using a plane-wave basis set," *Comput. Mater. Sci.* **6**(1), 15–50 (1996).

51. G. Kresse and J. Furthmüller, "Efficient iterative schemes for ab initio total-energy calculations using a plane-wave basis set," *Phys. Rev. B* **54**(16), 11169–11186 (1996).
52. G. Kresse and D. Joubert, "From ultrasoft pseudopotentials to the projector augmented-wave method," *Phys. Rev. B* **59**(3), 1758–1775 (1999).
53. S. Grimme, J. Antony, and S. Ehrlich, "A consistent and accurate ab initio parametrization of density functional dispersion correction (DFT-D) for the 94 elements H-Pu ARTICLES YOU MAY BE INTERESTED IN," *J. Chem. Phys.* **132**(15), 154104 (2010).
54. A. van de Walle, M. Asta, and G. Ceder, "The alloy theoretic automated toolkit: A user guide," *CALPHAD: Comput. Coupling Phase Diagrams Thermochem.* **26**(4), 539–553 (2002).
55. H. F. Le, C. R. Jeggo, G. D. Boyd, J. Appl, J. L. Shay, B. Tell, H. M. Kasper, L. M. Schiavone, H. Kasper, J. H. McFee, and B. F. Levine, Bond-Charge Calculation of Nonlinear Optical Susceptibilities for Various Crystal Structures, *Phys. Rev. B* **7**(6), 2600 (1971).
56. W. Zhu, F. He, J. Hayden, Z. Fan, J. I. Yang, J.-P. Maria, and S. Trolier-McKinstry, "Wake-Up in Al_{1-x}B_xN Ferroelectric Films," *Adv. Electron. Mater.* **8**(6), 2100931 (2022).